Electronic Supplementary Material (ESI) for Green Chemistry.

Boosting ammonia synthesis over MoO_2 by Li intercalation

Zhuoyang Gao,[1,3] Ruike Tan,[1,3] Ziye Pan,[1] Jiayang Li,[1] Qingyun Zhan,[1] Zhenlu Li,[1] Qingchuan Xiong,[2] Xiaoyue Mu,[2,*] Lu Li[1,2,*]

Affiliations:

[1]State Key Laboratory of Inorganic Synthesis and Preparative Chemistry, College of Chemistry, Jilin University, Changchun 130012, P. R. China

[2]College of Chemistry, Jilin University, Changchun 130012, P. R. China

[3]The authors contributed equally

*Correspondence to: xymu@jlu.edu.cn; luli@jlu.edu.cn

Materials and Methods

1. Materials.

Molybdenum oxide (MoO_2) was purchased from Alfa Aesar Co, Ltd. Iron(III) chloride ($FeCl_3$), lithium hydride (LiH), magnesium oxide (MgO), chloroplatinic acid hexahydrate ($H_2PtCl_6 \cdot 6H_2O$), ruthenium(III) chloride hydrate ($RuCl_3 \cdot xH_2O$), and tetrahydrofuran (THF) were purchased from Aladdin. Cobalt(II) chloride hexahydrate ($CoCl_2 \cdot 6H_2O$), nickel(II) chloride hexahydrate ($NiCl_2 \cdot 6H_2O$), absolute ethanol (AR grade), and concentrated hydrochloric acid (HCl) were purchased from Sinopharm Chemical Reagent Co, Ltd. The purities of H_2, N_2, and Ar gases are all 99.9995%.

2. General Characterization

The powder X-ray diffraction (XRD) patterns were performed on a Rigaku D/Max 2500/PV X-ray diffractometer with monochromator Cu Kα radiation (λ=1.5418 Å) from 10° to 80° with the scanning rate of 6°/min. Transmission electron microscopy (TEM) images, mapping images, were measured using a Tecnai G2 S-Twin F20 at the acceleration voltage of 200 kV. Scanning electron microscopy (SEM) and energy dispersive X-ray spectroscopy (EDS) analysis were collected using a Helios NanoLab 600I from FEI Company. X-ray photoelectron spectroscopy (XPS) was recorded on a Thermo ESCALAB 250 X-ray photoelectron spectrometer with a monochromated X-ray source (Al Kα $h\nu$=1486.6 eV). The energy scale of the spectrometer was calibrated using $Au4f_{7/2}$, $Cu2p_{3/2}$, and $Ag3d_{5/2}$ peak positions. The standard deviation for the binding energy (BE) values was 0.1 eV. Argon ion etch for one minute. Ultraviolet photoelectron spectroscopy (UPS) measurements were carried out by a Prevac spectrometer with a VG

Scienta R3000 hemispherical electron energy analyzer. Photons with energy of 21.22 eV generated by helium I were used for UPS spectra. The electron paramagnetic resonance spectra were obtained on a JES-FA 200 EPR spectrometer. The details of the instrumental parameters were as follows: scanning frequency: 9.45 GHz; scanning width: 800 mT; scanning power: 0.998 mW; scanning temperature: 293 K. Fourier transform infrared (FTIR) spectroscopy was performed on a Bruker VERTEX 80 V spectrometer. The Brunauer-Emmett-Teller (BET) surface areas of the samples were measured from the adsorption of N_2 at 77 K by using a Micromeritics ASAP 2020M system. Ferromagnetism was measured with a superconducting quantum interference device (SQUID, Quantum Design Inc.). Inductively coupled plasma (ICP) analyses were carried out on an iCAP 7600 ICP-OES instrument. The temperature-programmed desorption was performed on an Autochem II 2920 apparatus (Micromeritics, USA). Quantitative samples were usually loaded and pre-treated in an inert gas flow at 500 °C for 1 h. The samples were saturated with a flow of 25 mL min^{-1} 10% N_2 (or H_2)/He for 60 min. After being purged with inert gas for 1 h, the samples were heated from 50 °C to 500 °C with a heating rate of 10 °C/min under inert gas atmosphere, and the desorbed NH_3 (N_2, H_2) was determined using a thermal conductivity detector. Catalytic reactions were carried out over the WFSM-3060 catalyst evaluation system from Tianjin Xianquan Industry and Trade Development Ltd. Ammonia concentration was measured by ion chromatography (IC) on a PIC-10 produced by Qingdao Puren Instrument Ltd.

3. Kinetic calculations

If assuming the dissociation of N_2 ($N_2^* \rightarrow 2N^*$) as the rate-determining step:

$$r = \frac{\underset{k_4}{\rightarrow} K_2 P_{N_2}}{\left(1 + K_1 P_{H_2} + K_2 P_{N_2} + \sqrt{K_1 K_3 P_{H_2}}\right)^2} \quad (1)$$

If assuming the formation of NH (N* + H* → NH*) as the rate-determining step:

$$r = \frac{\underset{k_5}{\rightarrow} \sqrt{K_1 K_2 K_3 K_4} \sqrt{P_{H_2} P_{N_2}}}{\left(1 + K_1 P_{H_2} + K_2 P_{N_2} + \sqrt{K_1 K_3 P_{H_2}} + \sqrt{K_2 K_4 P_{N_2}}\right)^2} \quad (2)$$

Where $\overrightarrow{ki}$ is the rate constant of the forward reaction and *K*i is the equilibrium constant in step *i*.

4. Density Functional Theory (DFT) Calculations

The DFT calculations were performed by using the Vienna Ab Initio Simulation Package (VASP)[1,2] based on density functional theory (DFT)[3,4]. The exchange-correlation interaction adopted the generalized gradient approximation (GGA) with Perdew-Burke-Ernzerhof (PBE) functional[5]. The projector augmented wave (PAW) method[6,7] were used to describe the ion-electron interactions.

The energy cutoff of the plane-wave basis was set to 400 eV. The convergence criteria of the residual force and energy during the structure relaxation are set to 0.01 eV $Å^{-1}$ and 10^{-4} eV, respectively. We chose 4 × 2 × 1 Gemma k-points in the first Brillouin zone for geometric optimization and electronic structure calculation. The structure of bulk molybdenum(IV) oxide including four MoO_2 units was composed of a periodic supercell[8], which is used to construct the periodic plate of (011) surface calculations. The (011) surfaces were modeled by a three-layer plate containing Mo_8O_{16} each layer. Three models of MoO_{2-x}, Li-MoO_{2-x} and Fe@Li-MoO_{2-x} (the concentration of both oxygen vacancy and iron were set to be 1.408 %, and the concentration of lithium was evenly mixed at 16.901% were constructed. In order to avoid the interaction between two adjacent layers, a 15-Å-thick vacuum region was added along the z-axis. During

the optimization, the bottom two layers remained fixed, and the top layer and the adsorbent were completely relaxed.

The adsorption energies (E_{ad}) of molecule were defined as Equation (3):

$$E_{ad} = E_{total} - E_{surf} - E_{mole} \quad (3)$$

where E_{total},E_{surf}, and E_{mole} are the energies of adsorption configurations, slab models, and free gas molecules.

The formation Gibbs free energy (ΔG) in the reaction coordinate is calculated as Equation [9](4):

$$\Delta G = \Delta E + \Delta ZPE - T\Delta S \quad (4)$$

where ΔE is the adsorption energy, ΔZPE is the correction of zero-point energy and $T\Delta S$ is the entropy difference between the gas phase and adsorbed state. The zero-point energies and entropies of the reactive species are calculated from the vibrational frequencies at 673 K and 10 bar and the vibrational frequencies and entropies of molecules in the gas phase are taken from the NIST database [http://cccbdb.nist.gov/].

Differential Charge Density (DCD) was adopted to qualitatively evaluate the charge density difference $\Delta\rho(r)$, which can be defined as Equation (5):

$$\Delta\rho(r) = \rho_{Li-MoO_{2-x}}(r) - \rho_{MoO_{2-x}}(r) - \rho_{Li}(r) \quad (5)$$

where $\rho_{Li-MoO_{2-x}}(r)$ represents the total charge density of the fully relaxed configuration of Li-MoO_{2-x} surface.$\rho_{MoO_{2-x}}(r)$ and $\rho_{Li}(r)$ represent the total electronic charge densities of the separated MoO_{2-x} surface and doped lithium, respectively, which maintain the same geometrical structures as the relaxed configuration of Li-MoO_{2-x} surface.

All the transition states were determined using the climbing image-nudged elastic band (CI-NEB) method[10,11]. Four images were set in the elastic band between the initial and final states to calculate the

transition state (TS) configuration at the saddle point. The convergence criterion for energy is 10^{-7} eV and for force is 0.01 eV $Å^{-1}$.

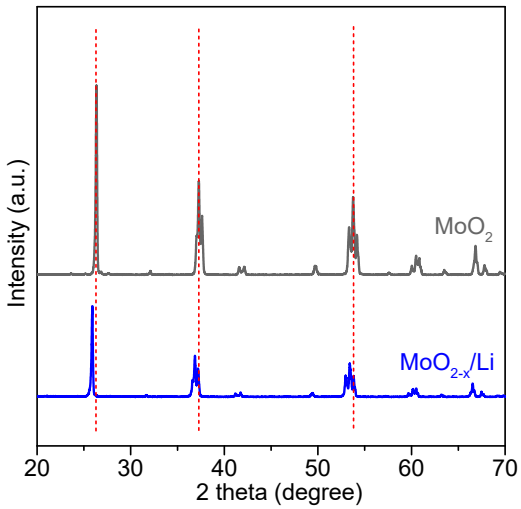

Fig. S1. Powder XRD patterns of MoO_2 and MoO_{2-x}/Li.

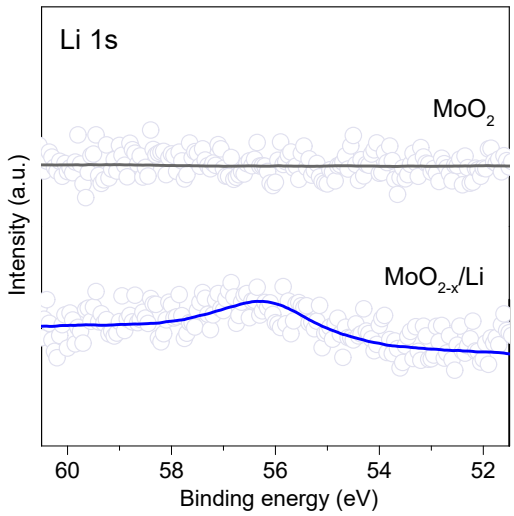

Fig. S2. XPS spectra of Li 1s for MoO_2 and MoO_{2-x}/Li.

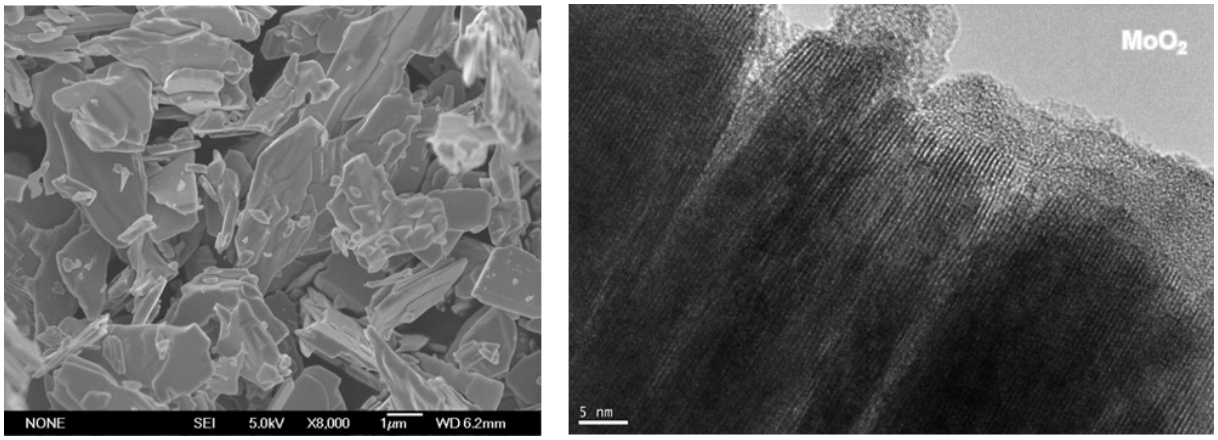

Fig. S3. SEM (left) and TEM (right) images of the MoO_2 sample.

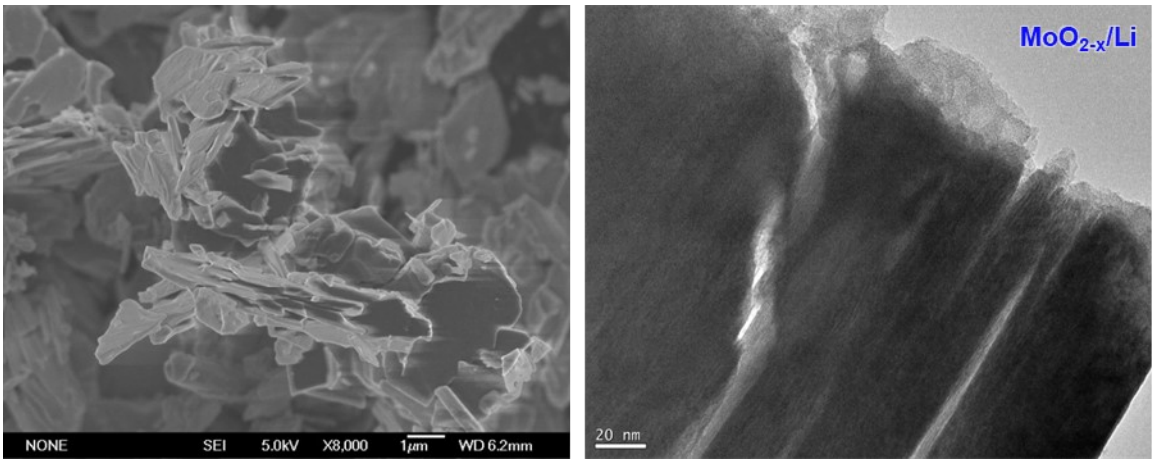

Fig. S4. SEM (left) and TEM (right) images of the MoO_{2-x}/Li sample.

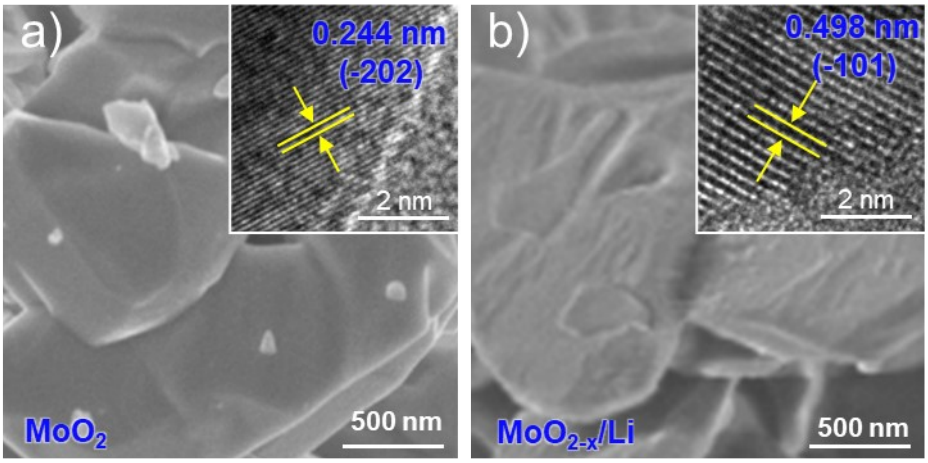

Fig. S5. SEM images of (a) MoO_2 and (b) MoO_{2-x}/Li. The insets show the corresponding HRTEM images.

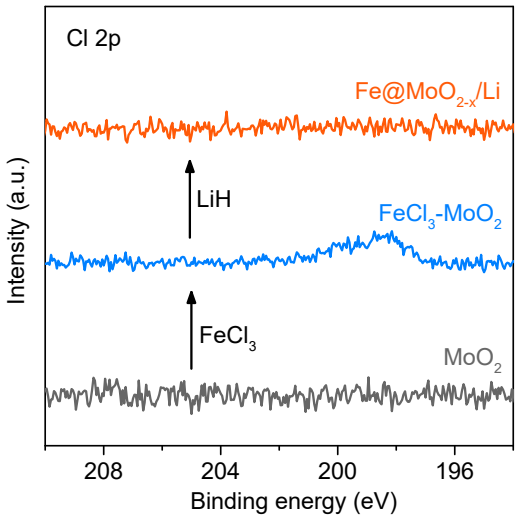

Fig. S6. XPS spectra of Cl 2p for MoO_2, $FeCl_3$-MoO_2 and Fe@MoO_{2-x}/Li.

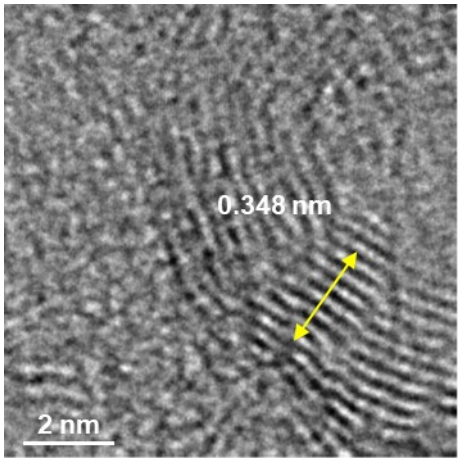

Fig. S7. HRTEM image of the multiple layers of the Fe@MoO_{2-x}/Li nanosheets.

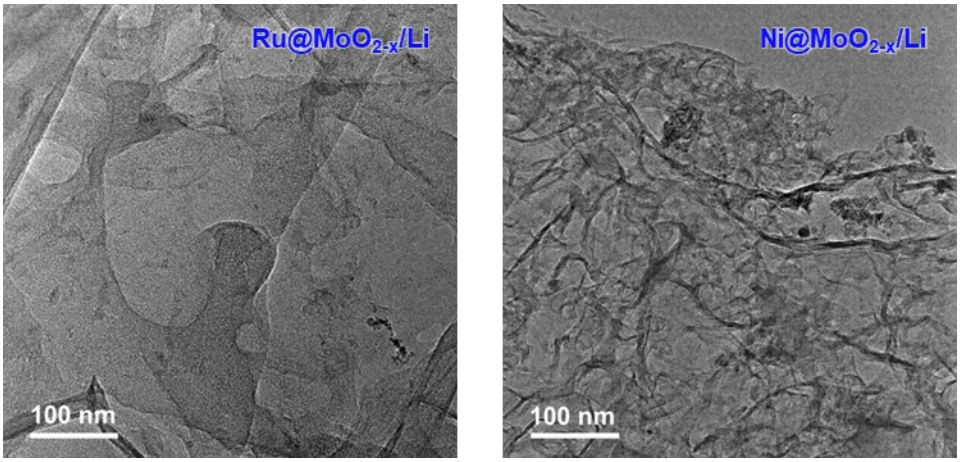

Fig. S8. TEM images of Ru@MoO_{2-x}/Li and Ni@MoO_{2-x}/Li.

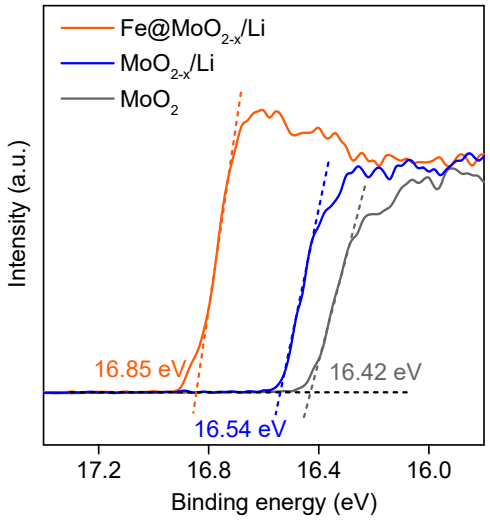

Fig. S9. UPS spectra of MoO_2, MoO_{2-x}/Li and Fe@MoO_{2-x}/Li.

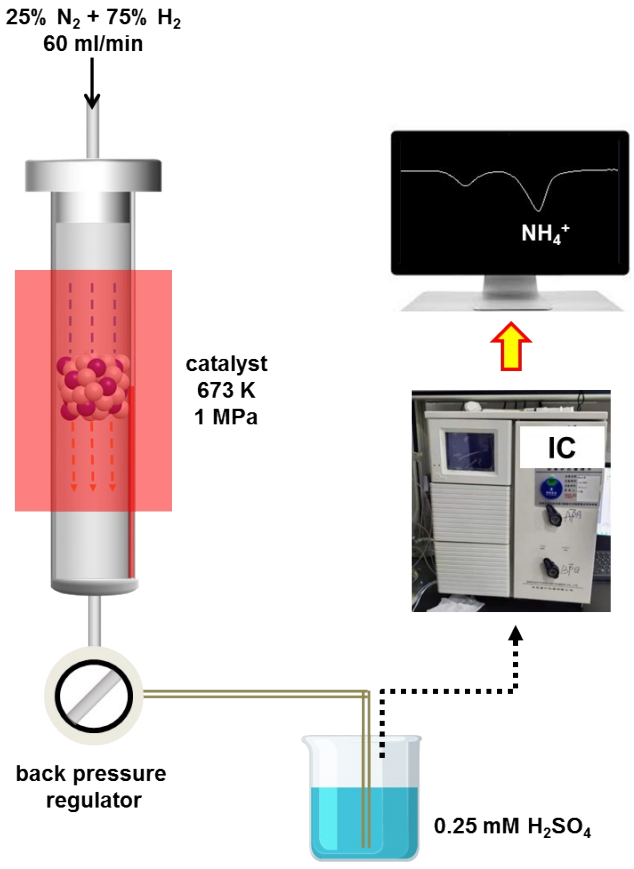

Fig. S10. Schematic diagram of the whole catalytic system.

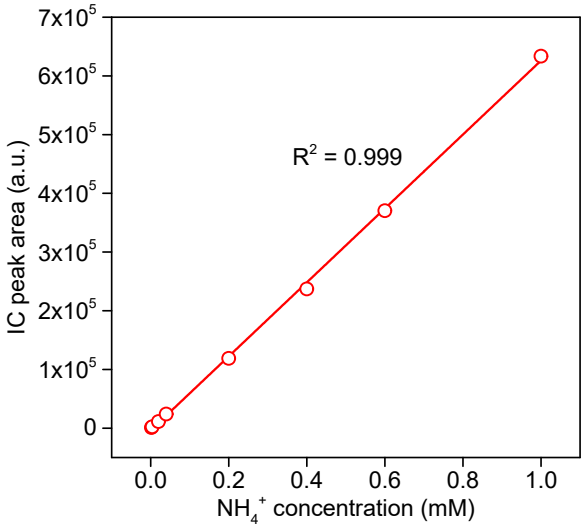

Fig. S11. The calibration curve of NH_4^+ using the ion chromatograph method.

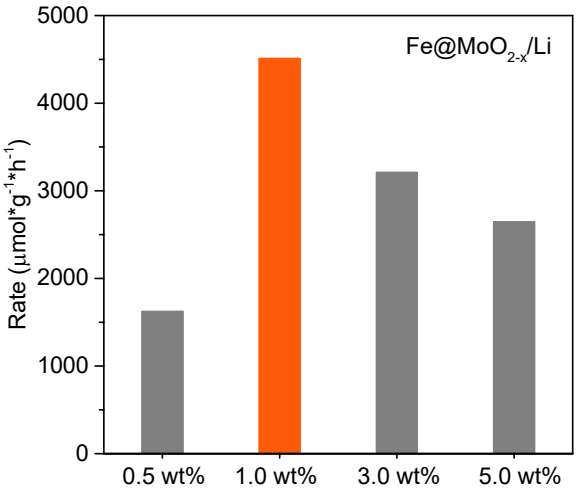

Fig. S12. Ammonia synthesis rate of $Fe@MoO_{2-x}/Li$ with different amount of Fe loadings.

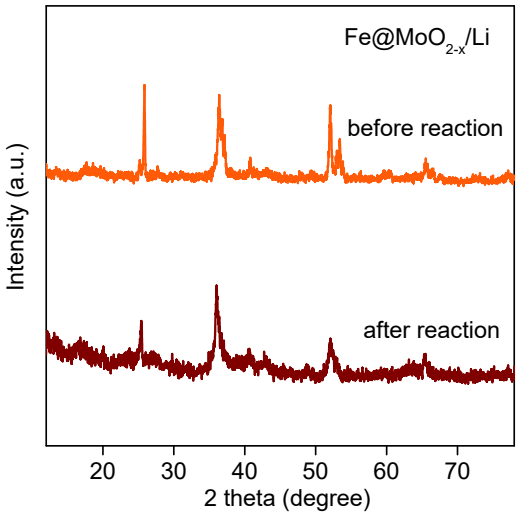

Fig. S13. Powder XRD patterns of a mixture of Fe@MoO_{2-x}/Li (30 mg) and quartz sand (500 mg) before and after the reaction.

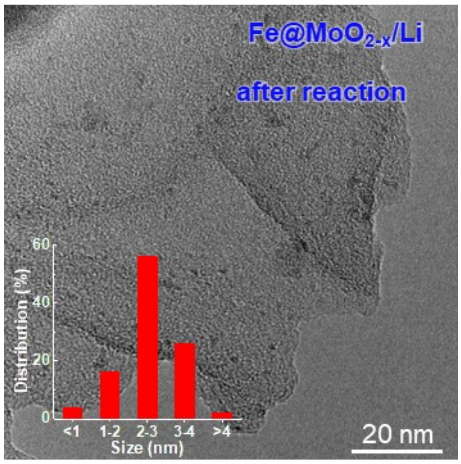

Fig. S14. TEM image of Fe@MoO_{2-x}/Li after the reaction. The inset histogram shows the diameter distributions of Fe nanoparticles.

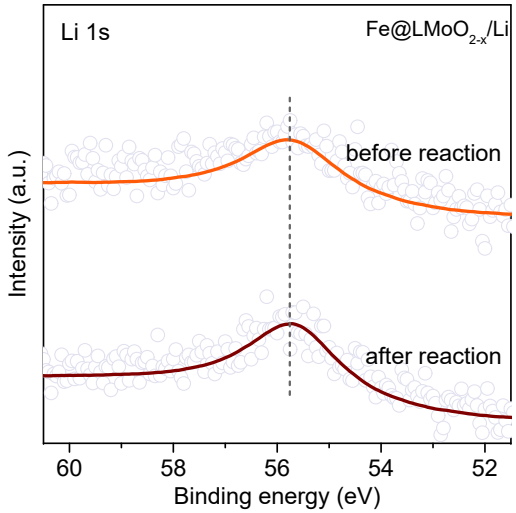

Fig. S15. XPS spectra of Li 1s for Fe@MoO_{2-x}/Li before and after the reaction.

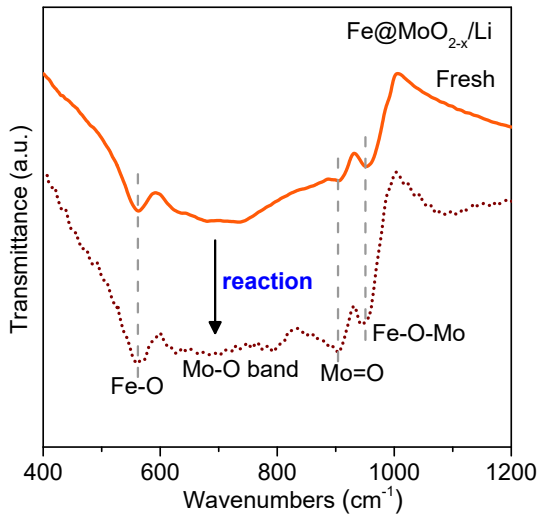

Fig. S16. FTIR spectra of Fe@MoO_{2-x}/Li before and after the reaction.

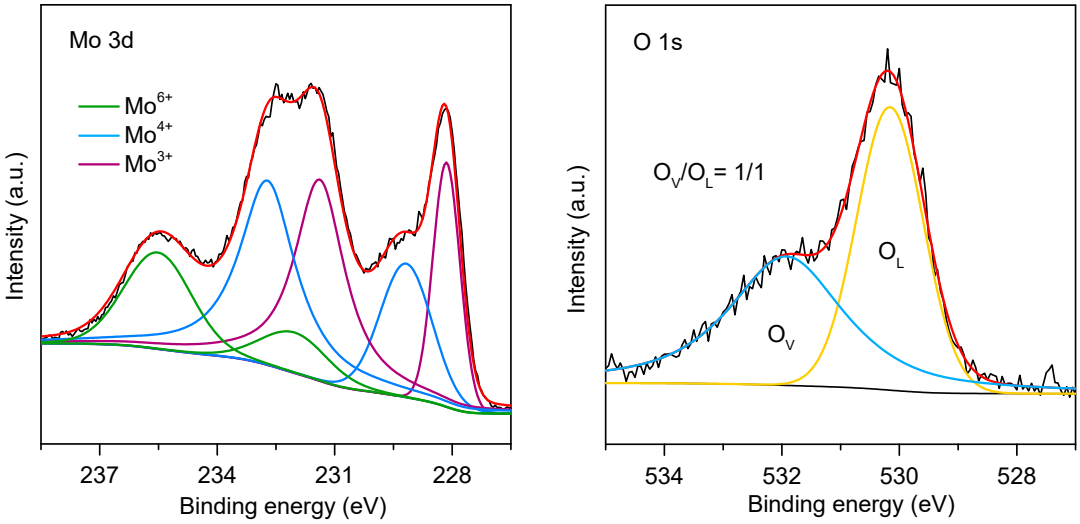

Fig. S17. XPS spectra of Mo 3d and O 1s for Li-free MoO_{2-x}.

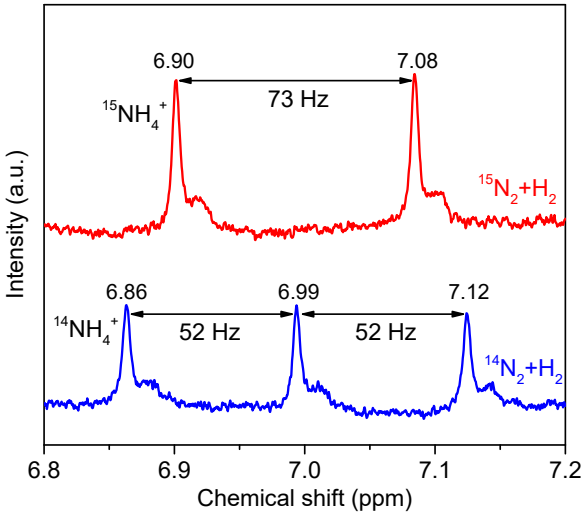

Fig. S18. ^{1}H NMR spectra (400 MHz) of both $^{15}NH_4^+$ and $^{14}NH_4^+$ produced from the reactions using $^{15}N_2$ or $^{14}N_2$ as the N_2 source.

$$N_2(g) \rightarrow N_2^*$$

$$H_2(g) \rightarrow H_2^*$$

$$N_2^* \rightarrow 2N^*$$

$$H_2^* \rightarrow 2H^*$$

$$N^* + H^* \rightarrow NH^*$$

$$NH^* + H^* \rightarrow NH_2^*$$

$$NH_2^* + H^* \rightarrow NH_3^*$$

$$NH_3^* \rightarrow NH_3(g)$$

Fig. S19. Elementary steps for ammonia synthesis based on Langmuir-Hinshelwood mechanism.

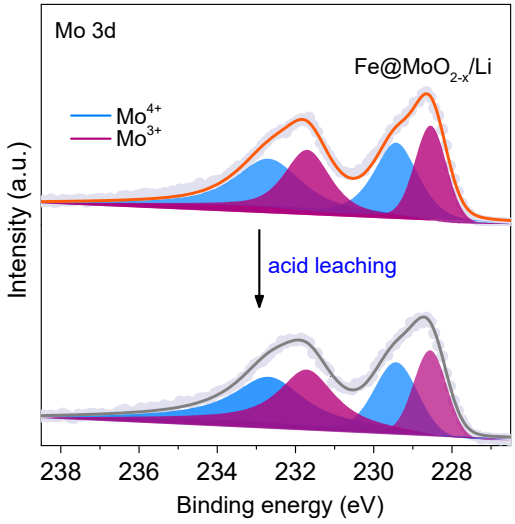

Fig. S20. XPS spectra of Mo 3d for Fe@MoO_{2-x}/Li before and after the acid leaching treatment.

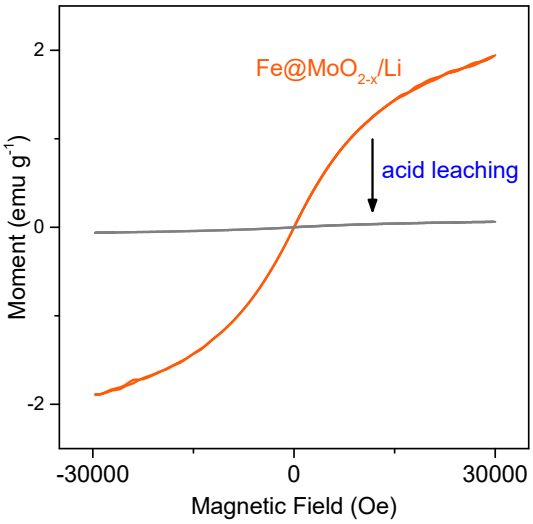

Fig. S21. Magnetization versus magnetic field (M-H) plots of Fe@ MoO_{2-x}/Li before and after the acid leaching treatment.

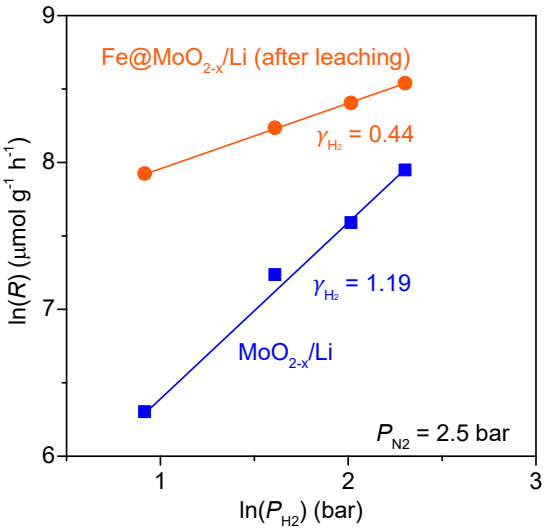

Fig. S22. Dependences of ammonia synthesis on the partial pressures of H_2

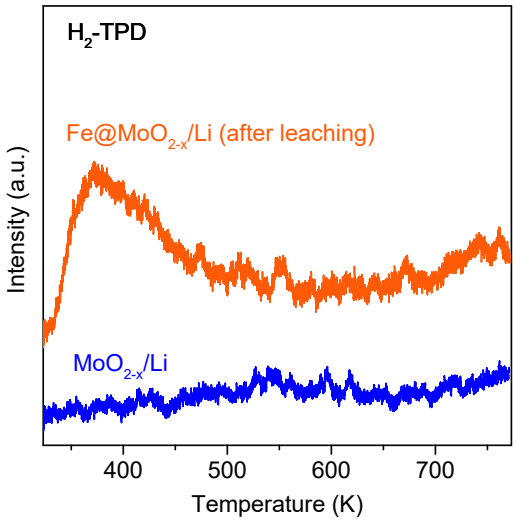

Fig. S23. H_2-TPD profiles of MoO_{2-x}/Li and Fe@ MoO_{2-x}/Li (after leaching).

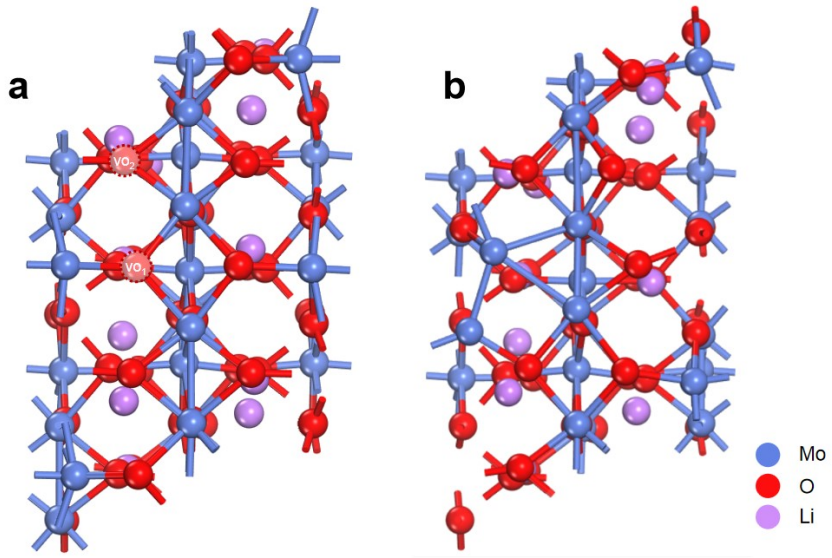

Fig. S24. (a) Two possible positions for oxygen vacancy. (b) The optimization model of optimal oxygen vacancy. Note: We choose the surface of Li-MoO_2 to model the two oxygen vacancies separately to find the best oxygen vacancy position. It is calculated that the slab energy of the model that forms oxygen vacancies at VO_2 position is -655.18 eV. The configuration that forms oxygen vacancies at VO_1 shows the lowest energy -656.06 eV, which has been applied in the further calculations.

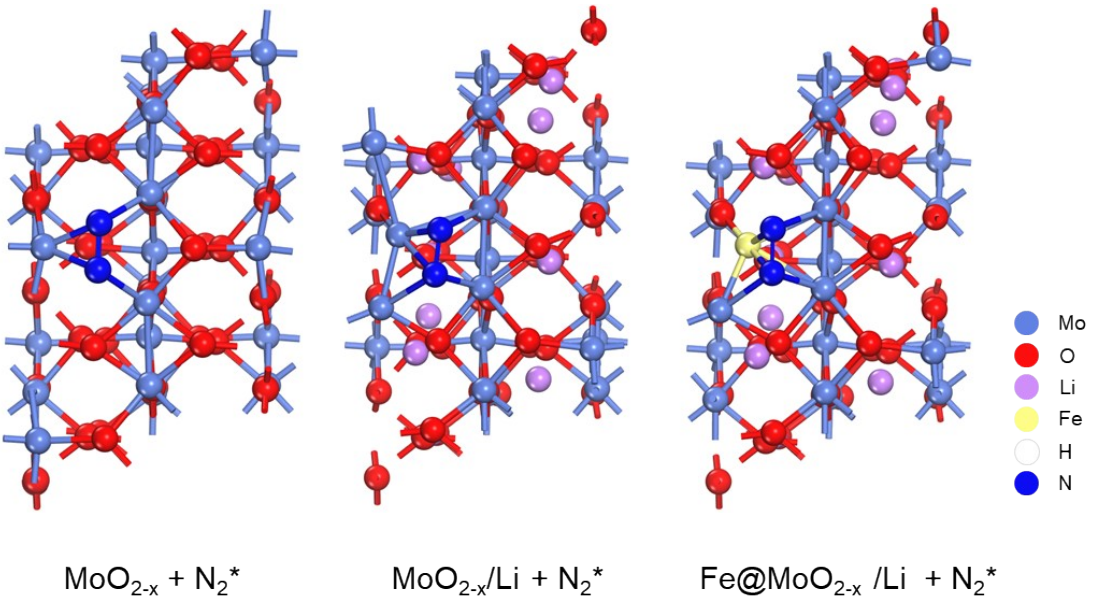

Fig. S25. The optimized configurations of N_2 adsorption on the models of MoO_{2-x}, MoO_{2-x}/Li and Fe@MoO_{2-x}/Li (after leaching).

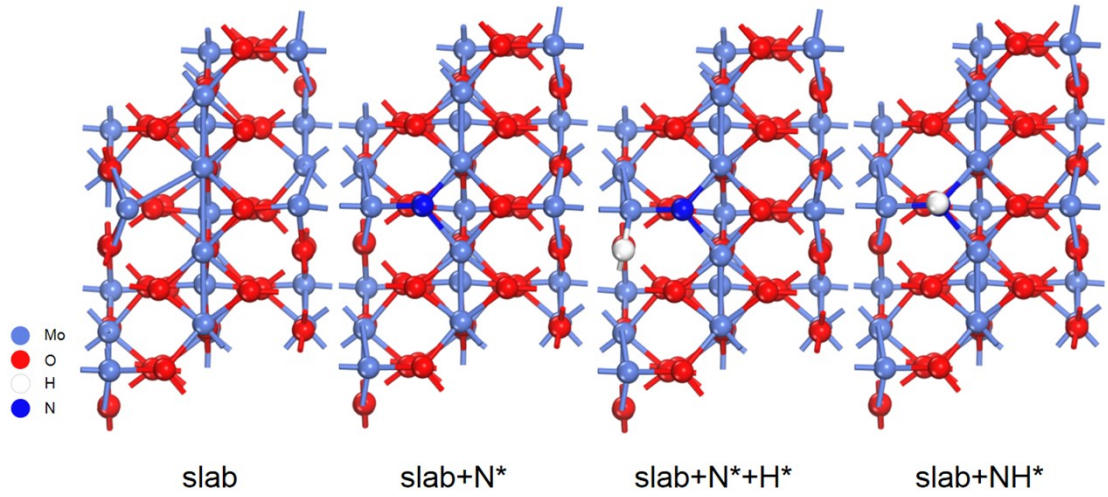

Fig. S26. The optimization model of MoO_{2-x} and the optimized configuration of N*, N*+H* and NH* adsorption on the model of MoO_{2-x}.

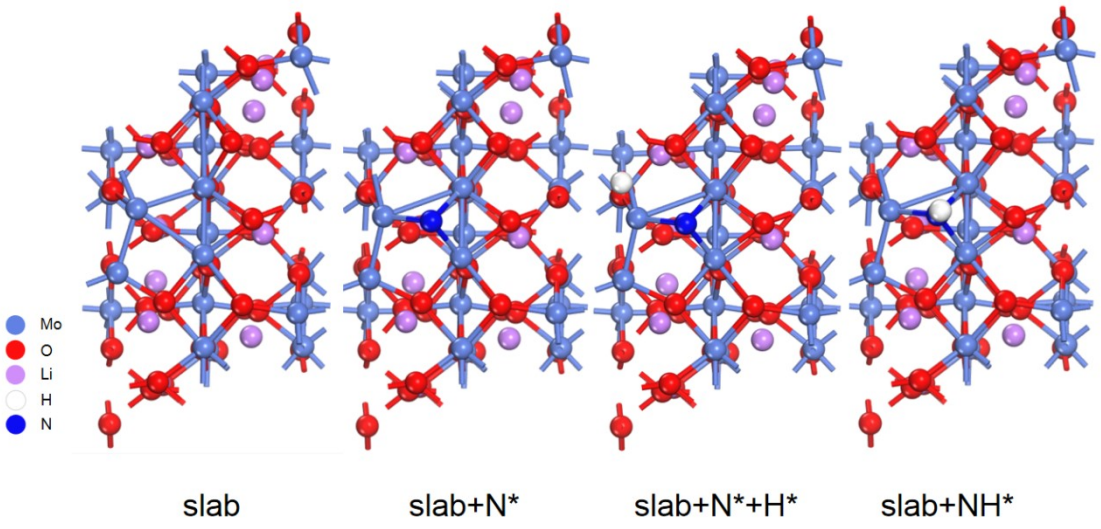

Fig. S27. The optimization model of MoO_{2-x}/Li and the optimized configuration of N*, N*+H* and NH* adsorption on the model of MoO_{2-x}/Li.

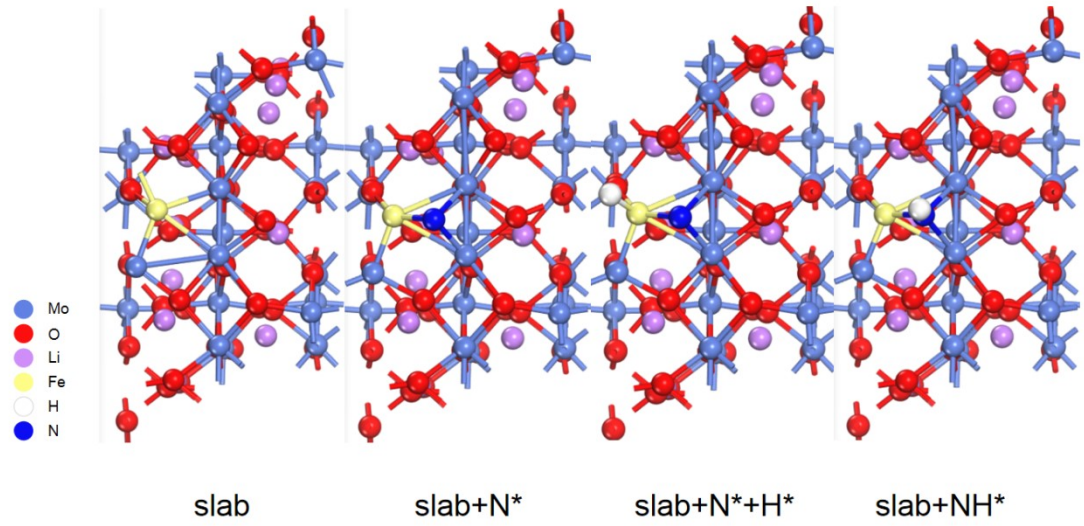

Fig. S28. The optimization model of Fe@MoO_{2-x}/Li (after leaching) and the optimized configuration of N*, N*+H* and NH* adsorption on the model of Fe@MoO_{2-x}/Li (after leaching).

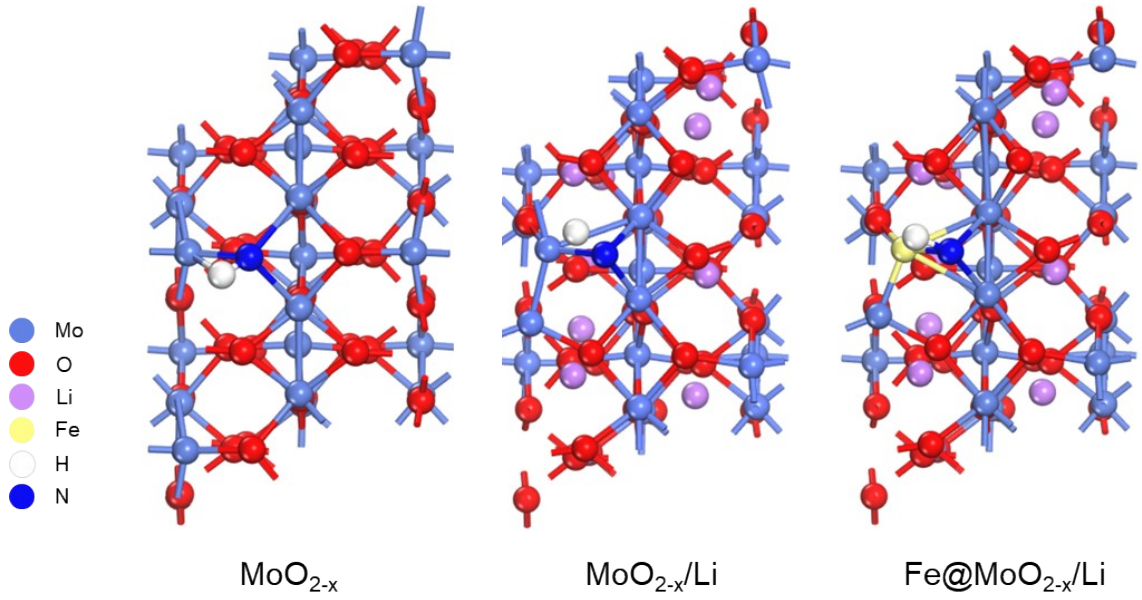

Fig. S29 The optimized configurations of transition states on the models of MoO_{2-x}, MoO_{2-x}/Li and Fe@MoO_{2-x}/Li (after leaching).

Table S1. Ammonia synthesis over recently developed catalysts

Catalysts	Temperature (°C)	Pressure (MPa)	flow rate (ml min^{-1})	RNH_3 (mmol g^{-1} h^{-1})	Ref.
Fe(1%)@MoO_{2-x}/Li	400	1.0	60	4.57	*This work*
Fe(0.1%)@MoO_{2-x}/Li (after acid leaching)	400	1.0	60	4.71	*This work*
Ni_2Mo_3N	400	0.1	60	0.39	12
Co_3Mo_3N	400	0.1	60	0.65	12
Fe-Mo-N	400	0.1	60	0.14	12
Fe-LiH	350	1.0	30	10.5	13
LaCoSi	400	0.1	60	1.25	14
LaCoSi	400	0.9	60	5.00	14
Ni-LaN bulk	400	0.1	60	2.40	15
Ni-LaN NPs	400	0.1	60	5.54	15
Cs-Ru (1%)/MgO	400	5.0	60	2.70	16
Ru(1%)/CeO_2-H	400	1.0	60	3.98	17
Ru(0.1%)/C12A7:e^-	400	1.0	60	0.99	18
Ru(1.2%)/C12A7:e^-	400	1.0	60	8.245	18
LaRuSi	400	0.1	60	1.76	19
Ru (12%)/CaFH	340	0.1	60	15	20
Cs-Ru (10%)/MgO	340	0.1	60	8.32	20

Reference

1. G. Kresse and J. Hafner, *Phys. Rev. B*. 1994, 49, 14251-14269.
2. G. Kresse and J. Furthmüller, *Phys. Rev. B.* 1996, 54, 11169-11185.
3. W. Kohn and L. J. Sham, *Phys. Rev.* 1965, 140, 1133-1138.
4. P. Hohenberg and W. Kohn, *Phys. Rev.* 1964, 136, 864-871.
5. J. P. Perdew, K. Burke and M. Ernzerhof, *Phys. Rev. Lett.* 1996, 77, 3865-3868.
6. P. E. Blochl, *Phys. Rev. B.* 1994, 50, 17953-17979.
7. G. Kresse and D. Joubert, *Phys. Rev. B.* 1999, 59, 1758-1775.
8. Renata Tokarz-Sobieraj, Robert Gryboś, Małgorzata Witko, *Appl. Catal. A: Gen.* 2011, 391(1-2):137-143.
9. A. A. Peterson, Energy Environ. Sci. 2010, 3, 1311-1315.
10. G. Henkelman and H. Jónsson, *J. Chem. Phys.* 2000, 113, 9978-9985.
11. D. Sheppard, R. Terrell and G. Henkelman, *J. Chem. Phys.* 2008, 128, 134106.
12. R. Kojuma and K. i. Aika, *Appl. Catal. A* 2001, **218,** 121-128.

13. P. Wang, F. Chang, W. Gao, J. Guo, G. Wu, T. He and P. Chen, *Nat. Chem.* 2017, **9**, 64-70.
14. Y. Gong *et al. Nat. Catal.* 2018, *1*, 178-185.
15. T. N. Ye, S. W. Park, Y. Lu, J. Li, M. Sasase, M. Kitano, T. Tada, and H. Hosono, *Nature* 2020, **583**, 391-395.
16. Y. Kobayashi, Y. Tang, T. Kageyama, H. Yamashita, N. Masuda, S. Hosokawa and H. Kageyama, *J. Am. Chem. Soc.* 2017, **139**, 18240-18246.
17. C. Li *et al. J. Energy Chem.* 2021, **60**, 403-409.
18. M. Kitano, Y. Inoue, Y. Yamazaki, F. Hayashi, S. Kanbara, S. Matsuishi, T. Yokoyama, S.-W. Kim, M. Hara and H. Hosono, *Nat. chem.* 2012, **4**, 934-940.
19. J. Wu *et al. Angew. Chem. Int. Ed.* 2019, 58, 825–829.
20. M. Hattori, S. Iijima, T. Nakao, H. Hosono and M. Hara, *Nat. Commun.* 2020, **11**, 2001.